Investigation of Deposition Parameters for Near-Beta Alloy Ti-55511 Fabricated by Directed Energy Deposition

Addison Rayner , Greg Sweet , Owen Craig , Mahdi Habibnejad-Korayem , Paul Bishop *

Posted Date: 8 March 2024

doi: 10.20944/preprints202403.0498.v1

Keywords: Directed energy deposition; Near-beta titanium alloys; Ti-55511; Plasma Atomized Powder

Article

Investigation of Deposition Parameters for Near-Beta Alloy Ti-55511 Fabricated by Directed Energy Deposition

A.J. Rayner [1], G.A.W. Sweet [2], O. Craig [1], M. Habibnejad-Korayem [3] and D.P. Bishop [1,*]

[1] Net Shape Manufacturing Group, Mechanical Engineering, Dalhousie University, Halifax, NS, B3H 4R2, Canada; addison.rayner@dal.ca (A.J.R.); ow728801@dal.ca (O.C.)
[2] Defence Research and Development Canada, Halifax, NS, Canada; greg.sweet@forces.gc.ca
[3] AP&C Advanced Powders and Coatings, Saint-Eustache, QC, J7R 0L5, Canada; mahdi.habibnejad@ge.com
* Correspondence: paul.bishop@dal.ca

Abstract: Directed energy deposition (DED) parameters were determined for near-β alloy Ti-55511 by employing statistical design of experiments (DOE) methods. Parameters resulting in fully dense freeform deposits were identified using two sequential DOEs. Single laser tracks were printed with several laser power, traverse rate, and powder feed rate settings in an initial DOE to identify promising build parameters. Capture efficiency and effective deposition rate were used to characterize and rank the single track deposits. The best parameters were then used to print solid cube with various X-Y and Z-overlaps (different hatch spacing, Hs, and layer thickness, Zs) in a second DOE. Suitable deposition parameters were selected based on cube density and microstructure and were used to fabricate larger tensile samples for mechanical testing. Multiple parameter sets were found to provide dense Ti-55511 deposits with acceptable mechanical properties and parametric models showed statistical significance.

Keywords: Directed energy deposition; Near-beta titanium alloys; Ti-55511; Plasma Atomized Powder

1. Introduction

Directed energy deposition (DED) is a form of additive manufacturing (AM) which can print complex net shape parts from a wide range of metal alloys. It offers fast prototyping, high build rates, dense materials, and the ability to tailor build parameters to obtain microstructurally and compositionally graded components [1–3]. As an AM technique, it can be leveraged for geometrical design, lightweighting, and part consolidation opportunities [3]. DED can also be used to deposit material on damaged or worn parts, effectively weld-repairing parts to extend service life [2–4]. As a result, DED of titanium alloys has the potential to reduce the lead time and buy-to-fly ratio of titanium aerospace components compared to wrought-based manufacturing processes [5,6]. Most research on DED of Ti alloys has been directed toward alpha and alpha + beta alloys, such as Ti-6Al-4V [5–12]. While AM of these materials has been largely successful, near-beta alloys such as Ti-5553 and Ti-55511 exhibit superior fracture toughness, are readily heat treatable, and are gaining popularity in the aerospace sector [13,14]. Accordingly, open literature on the development of AM techniques for near-beta Ti alloys is starting to emerge [5,6,15–17].

In DED, metal power feedstock is blown in the path of a focused laser which melts both the substrate and powder to form a consolidated deposit. The melt pool rapidly solidifies as the laser passes across the workpiece, leaving behind a dense bead of deposited material. The tool path of the laser can be designed to clad surfaces or build complex, freeform deposits of custom geometry. The laser spot size, laser power, traverse rate, powder feed rate, hatch spacing, and layer thickness are all significant variables which impact the deposition process and can interact with one another.

 doi:10.20944/preprints202403.0498.v1

Understanding the effect of each variable and their interactions on the deposition process is not always intuitive and is often material specific.

Generally, achieving full density is critical for materials manufactured using metal powder as feedstock. Internal porosity in the final material can act as stress risers and aid crack propagation under load, lowering the mechanical strength of the material. No significant correlation has been observed to relate the final density of DED printed materials to the starting porosity in the powder feedstock. However, the formation of defects in DED (inter-layer and intra-layer) are known to be a product of poor processing conditions [1–3]. The density of a given DED material is then related to the complex deposition parameters and their interaction effects. For example, Sweet et al., showed that slower traverse rates could be used to achieve high densities in a DED dual phase steel when the hatch spacing was large, while the traverse rate needed to be increased to achieve dense deposits when the hatch spacing was decreased [18]. Although multiple combinations of deposition parameters can lead to dense deposits, optimizing the global process parameters to avoid defect formation and maximize density remains challenging.

When a response of interest in a process, such as density, is known to be influenced by multiple factors, design of experiments (DOE) methods are commonly employed to optimize that process response [19]. Central composite, box-Behnken, and Taguchi method approaches have all been employed to optimize AM processes such as laser powder bed fusion and DED for a variety of responses (i.e., density or tensile strength) [20–25]. In this work, a statistical central composite design response surface method was selected to determine the main influence and interactions of DED process parameters and identify the best combination of parameters that produce a high density material. Utilizing this approach allows for a wide variety of deposition parameters to be examined while keeping the required number of test specimen low [18,19,22,25,26].

During deposition, residual stresses build up in the material due to the cyclic heating inherent to the DED process [2,3]. Since the volume of material being melted by the laser spot is very small compared to the substrate, the cooling and solidification rates are very high [2,3]. This results in a fine microstructure that increases the tensile strength but generally reduces ductility [27]. Therefore, the deposition parameters applied not only influence the material density, but the microstructure and residual stresses in the deposit as well. Additionally, anisotropy of the as-built part is reported across the literature regardless of the alloy system used. This anisotropy affects tensile properties and is closely related to the cyclic heating profile and build orientation during deposition [11,12,28–32]. As a result, heat treatment of DED materials is required to address residual stresses, microstructure, and mechanical properties.

Titanium has a hexagonal closed-packed (HCP) structure, referred to as the alpha phase, α, at room temperature. At the beta transus temperature (~885°C), titanium undergoes an allotropic transformation to the body centered-cubic (BCC) beta phase, β [13]. The addition of β-stabilizing elements such as Mo, V, Fe, and Cr tend to lower the beta transus temperature, allowing the metastable β-phase to be retained below the β transus temperature [13,14,33]. In contrast, α-stabilizing elements, such as Al, increase the β transus temperature and promote the formation of α. α+β Ti-alloys contain a mixture of α and β phase stabilizers and are heat treatable. Their properties are typically controlled through a solution heat treatment followed by aging between 480°C-650°C to form fine α and β in a matrix of retained β [13]. This bi-modal microstructure combines the strength from the α-phase and ductility from the β-phase [34]. In contrast, near-β Ti-alloys contain larger amounts of BCC-β phase stabilizers and respond more favourably to heat treatment [13]. Similar solutionizing and aging treatments can be applied to retain the β-phase while precipitating a fine dispersion of α particles which strengthen the alloy.

Studies on DED of near-β alloys are limited in the literature. Liu et al., investigated the mechanical properties and beta heat treatment of DED Ti-55511 in two studies [5,6]. Fine primary and secondary α phases were observed within the β grains of the as-deposited material and as a continuous α-phase along the grain boundaries. This microstructure increased the as-printed material's tensile strength, but decreased the ductility as crack nucleation and propagation was localized in the grain boundary α-phase [5]. Liu et al., highlight that in wrought forms of near-β

 doi:10.20944/preprints202403.0498.v1

alloys, forging treatments can easily remove or transform the detrimental grain boundary α phase [6]. However, AM is a net-shape process, making heat treatment the only option to address detrimental microstructural features. Heat treating the alloy above the β-transus temperature (~880°C in AM Ti-55511 [6]) for a short time will transform the undesired grain boundary α while limiting β grain growth, resulting in improved ductility while retaining high strength [6]. Deng et al., studied the mechanical properties of DED Ti-55531 in the as-built and heat treated conditions [35]. In their work, the former exhibited low tensile strength and high elongation. β-heat treatment at 880°C increased the tensile strength but resulted in a brittle fracture mode. In contrast, when the heat treatment at 880°C was followed by a secondary α/β-heat treatment at 790°C, a bimodal microstructure of primary and secondary α phase formed and resulted in a ductile fracture mode. Gosse also reported improvements to the tensile strength of DED Ti Beta 21S and Ti-6242 when their respective heat treatments were applied [26]. In their work, solution treatment of Ti Beta 21S at 843°C followed by aging at 679°C caused a decrease in yield strength, but a significant increase in ductility due to the formation of intergranular acicular α which restricted dislocation movement.

It is evident from the existing literature on DED of Ti-55511 and similar alloys that the as-deposited microstructure is commonly sub-optimal and must be remedied through a β-heat treatment, at minimum. The objective of the present study is to evaluate the freeform fabrication of near-beta alloy Ti-55511 and identify promising deposition parameters using DED. This work began with a statistical design of experiments (DOE) approach to rapidly infer build parameters which could fabricate dense deposits, followed by metallurgical and mechanical evaluation of the as-printed and heat treated specimens.

2. Materials and Methods

The powder used for DED in this study was a plasma atomized Ti-55511 (Ti-5Al-5Mo-5V-1Cr-1Fe) powder produced by AP&C. The particle size distribution (PSD) of the powder was measured by laser light scattering (Malvern Mastersizer 3000) and is presented in Figure 1a. The powder exhibited a D_{50} of 81 µm and had a size distribution that lied within the -150 µm/+50 µm range as is commonly specified for DED applications [2,3]. A representative SEM micrograph of the powder is presented in Figure 1b which confirmed its highly spherical morphology and a limited presence of satellite features. The powder chemistry (Table 1) was tested using inductively couple plasma—optical emission spectroscopy (ICP-OES) analysis and was confirmed to be compliant with the compositional ranges reported for Ti-55511 from GOST 19807:1991 [36].

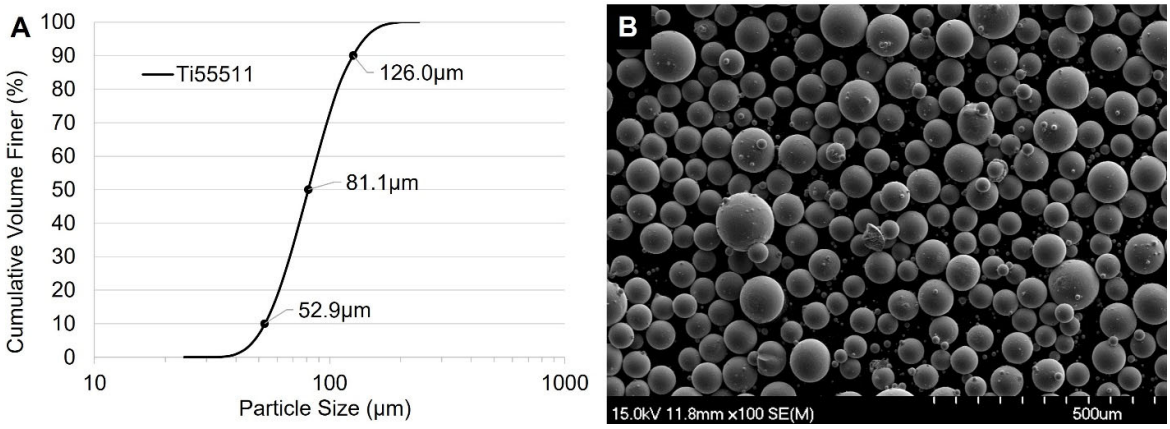

Figure 1. a) Particle size distribution of the plasma atomized Ti-55511 powder utilized and, b), SEM micrograph of the powder.

 doi:10.20944/preprints202403.0498.v1

Table 1. Composition of the gas atomized Ti-55511 powder compared to the wrought alloy composition from GOST 19807: 1991 [36].

	Composition (wt%)					
Material	Al	Cr	Fe	Mo	Ti	V
GOST 19807:1991	4.4-5.7	0.5-1.5	0.5-1.5	4.0-5.5	Bal.	4.0-5.5
Measured	5.38	1.05	1.07	4.95	82.40	5.14

DED Ti-55511 specimens were produced using an Optomec MTS 500 system equipped with a 1 kW Ytterbium-doped fiber laser (IPG Photonics; λ = 1070 nm) with a spot size of 600μm and a nozzle stand off distance of 6.12mm. All build cycles were executed under a fully enclosed argon atmosphere with a measured oxygen content <20 ppm (EOS-1 zirconia oxygen sensor, Inert Corp.). Each layer consisted of an in-fill using a 90-degree alternating hatch approach. No boundary layers were deposited. Mastercam Mill 2019 software coupled with a proprietary DED add-on was utilized to slice the 3D models and generate the required toolpaths. All builds were fabricated on Ti-6Al-4V (Ti-64) substrate plates. Each build plate was solvent degreased and abrasive grit blasted with 300 μm zirconia shot prior to use.

Two central composite designs (CCDs) were used to infer DED build parameters which could provide dense, defect free deposits of Ti-55511. Minitab 19 statistic software was utilized to create DED parameter sets for both CCDs and perform statistical analysis of the results. In the first CCD, the DED parameters of laser power, powder feed rate and traverse rate were evaluated for 20 single track deposits. The parameters tested are outlined in Table 2 and were evaluated at 5 discrete levels where level 3 represented the center point of the design (the condition to which the significance of changes was tested). The center point of the CCD was repeated 6 times. Laser confocal microscopy and optical microscopy were employed to analyze the resulting bead geometry and quality, respectively. The capture efficiency and effective deposition rates were determined based on the measured bead geometries and the sum of their respective rankings was used to determine an overall rank for each of the DED parameter sets considered.

Table 2. Machine parameters and levels used in the CCD for single track depositions.

Parameter	Levels				
	1	2	3	4	5
Laser Power (W)	350	391	450	509	550
Traverse Rate (mm/s)	10.0	11.2	13.0	14.8	16.0
Powder Feed (g/min)	0.5	1.0	1.7	2.4	2.9

A second CCD was used to evaluate the influence of hatch spacing, H_S, (XY step size) and layer thickness, Z_S, (Z-step size) on solid cube specimens built utilizing the best three, defect free parameter sets identified in the first CCD. A percentage overlap was used to calculate H_S and Z_S for each cube based on the respective single track bead width and height from condition 4, 5, or 9. These new parameter sets, outlined in Table 3, were applied to each of the top 3 ranked parameter sets from the first CCD. A total of 39 cubes were built, 13 for each condition (4, 5, or 9) testing different XY and Z overlaps. Each of the DED parameter sets evaluated in the CCDs were investigated at five discrete levels where level 3 represented the center point of the design. The centre point of each CCD was repeated 5 times.

Table 3. Machine parameters and levels used in the second CCD for cube specimen deposition.

Parameter	Levels				
	1	2	3	4	5
XY Overlap (%)	0	10	35	60	70
Z Overlap (%)	-32.5	-20	10	40	52.5

 doi:10.20944/preprints202403.0498.v1

A vertical band saw was used to remove the cube specimens from the Ti-64 build substrate. The density of each cube was then measured according to MPIF standard 42 [37]. Following density measurement, the cubes were sectioned vertically in half using a cut-off saw. Coolant used during cutting was removed from the cube specimens by immersing them in petroleum ether for a minimum of 1 hour. One half of the cube specimens was mounted in conductive Bakelite such that the viewing direction was perpendicular to the X-Z plane. A Struers Tegramin 20 auto polisher was used to prepare samples for metallography using progressively finer SiC foils, a 9µm diamond suspension, and finally, a 10:1 mixture of colloidal silica and hydrogen peroxide. Polished Ti-55511 specimens were immediately etched with Kroll's reagent to reveal the beta phase. Microstructures of the etched specimens were examined using a Keyence VK-X1000 laser confocal microscope.

Rectangular blanks of Ti-55511 with dimensions of 10 mm x 10 mm x 85 mm were built using two of the DED parameter sets identified. Each blank was machined into a cylindrical-gauge tensile specimen compliant with MPIF standard 10 [38]. A 1MN Instron load frame (model 5594-200HVL) equipped with a 50kN load cell was used to perform tensile tests. Strain was measured using an Epsilon 3542 extensometer which remained attached to the specimen through the point of fracture. All bars were stress relieved at 960°C for 1 hour under high vacuum in a Materials Research Furnaces Inc. (MRF) furnace prior to machining and tensile testing. The oxygen and nitrogen (ON) content of the tensile samples were measured using an Eltra Elementrac ONH-p2 analyzer.

3. Results and Discussion

3.1. Single Tracks

The top view and a polished cross section of a representative single track from the first CCD are presented in Figure 2A and 2B, respectively. Polished cross sections of the single tracks were analyzed using optical microscopy to identify any visible deposition defects (i.e., pores, lack of fusion, cracks, etc.) and characterize the amount of dilution. Track 20, shown in Figure 2, contained no internal defects and had approximately 50% dilution (where dilution is the ratio of the depth of penetration to the depth of penetration plus the bead height [3]). The topography of each track was analyzed using laser confocal microscopy to determine the bead geometry and cross-sectional area. For the track presented in Figure 2, the bead width and height were found to be 1360µm and 181µm, respectively, while the cross-sectional area was 147000 μm^2.

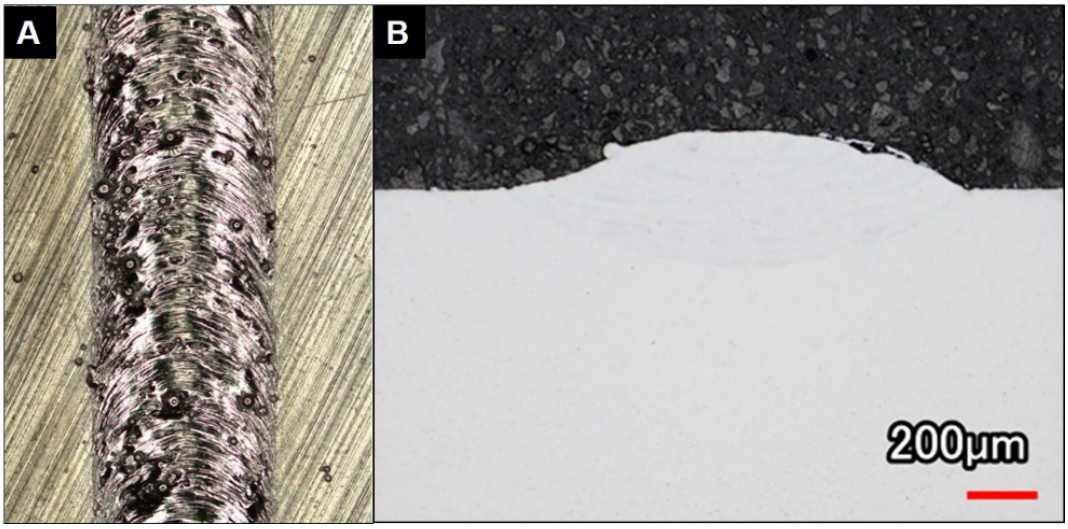

Figure 2. DED single track of Ti-55511 (Track 20: 450W;1.7g/min;13mm/s) a) As-deposited top view and b) polished cross section.

 doi:10.20944/preprints202403.0498.v1

The cross sectional area was used to calculate the capture efficiency and effective deposition rate for each single track deposit via Equations 1 and 2. Note that a 100% capture efficiency refers to all blown powder being captured in the deposited bead.

$$Capture\ Efficiency(\%) = \frac{Powder\ Captured}{Powder\ Used} = \frac{C.S.\ Area\ (mm^2) \times \rho_{Ti55511}(\frac{g}{mm^3})}{Powder\ feed\ \left(\frac{g}{min}\right) \div TraverseRate\ (\frac{mm}{min})} \quad (1)$$

$$Effective\ Deposition\ Rate\ \left(\frac{\text{g}}{\text{min}}\right) = \text{Capture Efficiency (\%)} \times Powder\ feed\ (\frac{g}{min}) \quad (2)$$

The capture efficiency and effective deposition rates were determined for each track and used to rank the associated parameter sets as shown in Table 4. Single tracks which contained defects were not selected for further evaluation. Both tracks 4 and 14 achieved the highest ranking followed by track 9. These tracks had capture efficiencies above 34% and deposition rates above 0.5 g/min. Track 5 was identified as the best low power candidate, having a similarly high capture efficiency to tracks 4, 14, and 9, but a slower deposition rate. Despite tracks 4 and 14 both being ranked highest, only track 4 was selected for further testing due to its significantly higher deposition rate and lower power. Based on this ranking, parameter sets for tracks 4, 5, and 9 were selected for testing in a second CCD of cube deposits.

Table 4. Single track CCD results and overall ranking based on capture efficiency, effective deposition rate, and presence of defects.

Track	Laser Power (W)	Traverse Rate (mm/s)	Powder Feed (RPM)	Capture Efficiency		Effective Deposition Rate		Sum	Overall Rank
				(%)	(Rank)	(g/min)	(Rank)		
1	450	13.0	1.50	21%	16	0.36	14	30	17
2	391	11.2	2.25	22%	15	0.54	6	21	10
3	391	14.8	0.75	30%	10	0.30	19	29	16
4	**509**	**11.2**	**2.25**	**37%**	**4**	**0.90**	**1**	**5**	**1**
5	**391**	**11.2**	**0.75**	**34%**	**8**	**0.33**	**17**	**25**	**12**
6	509	14.8	2.25	20%	17	0.49	10	27	15
7	450	13.0	1.50	29%	11	0.50	8	19	9
8	450	13.0	2.76	29%	12	0.85	2	14	6
9	**450**	**13.0**	**1.50**	**34%**	**6**	**0.59**	**4**	**10**	**3**
10	450	13.0	1.50	34%	7	0.59	5	12	4
11	391	14.8	2.25	14%	20	0.35	15	35	19
12	450	13.0	1.50	29%	13	0.49	9	22	11
13	450	13.0	0.24	36%	5	0.17	20	25	12
14	**550**	**13.0**	**1.50**	**38%**	**2**	**0.65**	**3**	**5**	**1**
15	509	14.8	0.75	43%	1	0.42	12	13	5
16	450	16.0	1.50	19%	19	0.32	18	37	20
17	509	11.2	0.75	37%	3	0.36	13	16	7
18	450	10.0	1.50	27%	14	0.46	11	25	12
19	350	13.0	1.50	20%	18	0.34	16	34	18
20	450	13.0	1.50	31%	9	0.53	7	16	7

The effects and interaction effects of the single track parameters (laser power, traverse rate, powder feed rate) on the capture efficiency and deposition rate were modeled using Minitab and analyzed by ANOVA. A stepwise approach was employed and a level of significance of 0.05 was used to test individual terms, their squares, and their interactions. Low p-values ($p < 0.001$) and insignificant lack-of-fit tests ($p > 0.05$) in both cases suggested the models were statistically suitable

 doi:10.20944/preprints202403.0498.v1

to predict the deposition response for single tracks. The adjusted R-sq values were 68.0% and 78.2% for the capture efficiency and deposition rate models, respectively. Contour plots of the modeled single track deposition behaviour are presented in Figure 3. The capture efficiency plots (left column, Figure 3) indicated that higher laser powers and lower powder feed rates led to higher capture efficiencies. Mid-range traverse rates also appeared to provide higher capture efficiency at low laser powers and high powder feed rates, but traverse rate became less important as the laser power was increased. The deposition rate followed similar behaviour to the capture efficiency, however the deposition rate increased as the powder feed was increased. The selected tracks (4, 5, 9) had predicted deposition rates between 0.4-0.8 g/min while the capture efficiency predictions were confined to a mid-range of 25-35%. Note that these contour plots do not provide any information about how the tested machine parameters influence the density of the deposited beads.

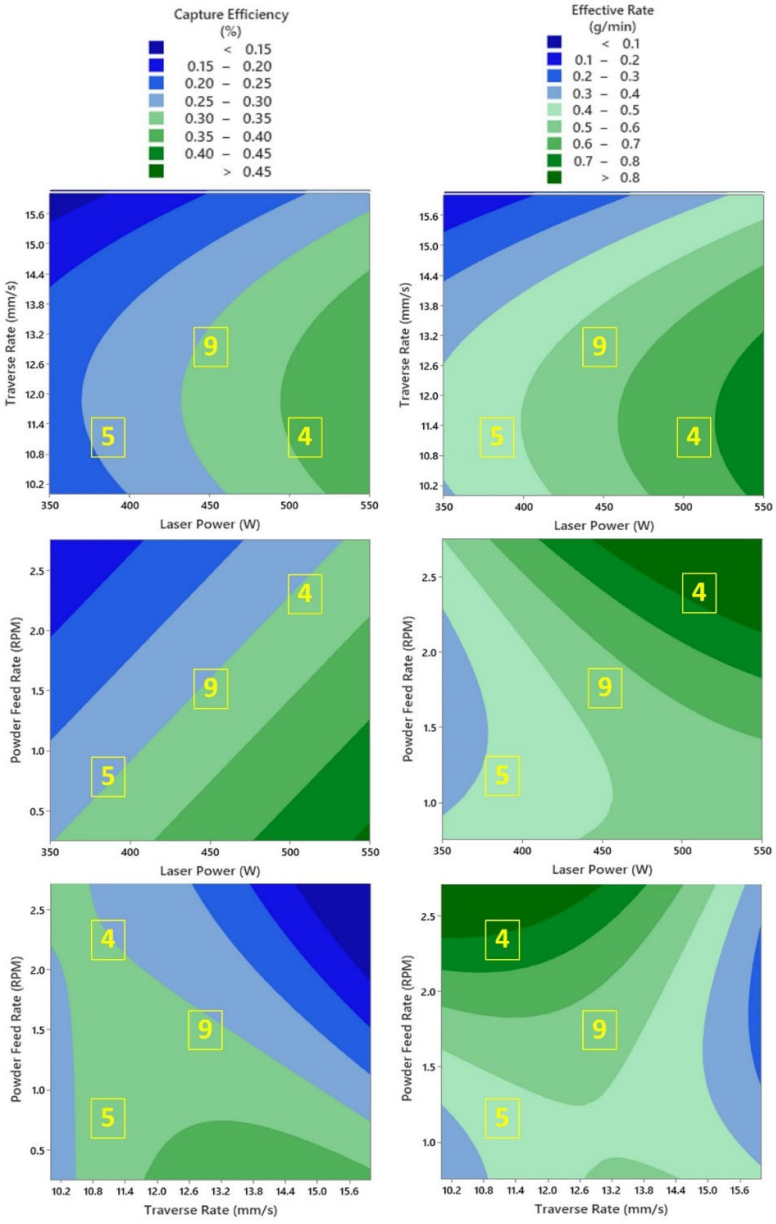

Figure 3. Contour plots of the capture efficiency (left column) and effective deposition rate (right column) for machine parameters used to deposit single tracks of Ti-55511. Parameters for tracks 4, 5, and 9 are highlighted.

 doi:10.20944/preprints202403.0498.v1

3.2. Solid Cube Characterization

Solid cubes with different X-Y and Z-overlaps were built in a second CCD according to Table 3 using the selected machine parameters from the single track CCD (conditions 4, 5, and 9). The density and microstructure of the cube specimens were analyzed and compared against a full theoretical density of 4.642 g/cm^3 for Ti-55511. As-deposited cubes of Ti-55511 are shown in Figure 4.

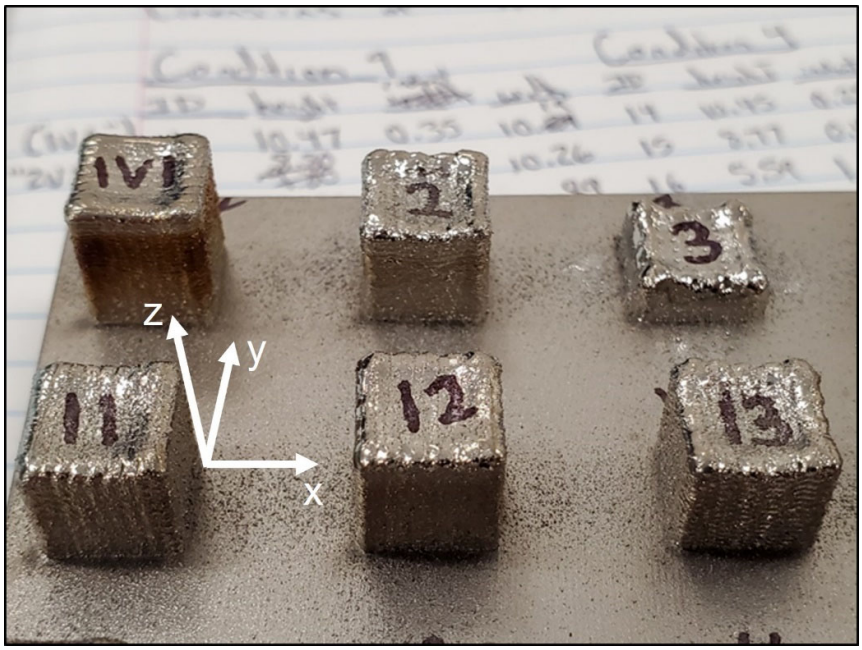

Figure 4. Examples of DED cube specimens of Ti-55511 deposited as part of the second CCD. Cubes are approximately 10x10mm in the XY plane and exhibit different build heights.

AM parameters are commonly simplified into a singular energy input parameter such as linear heat input [1]. However, this approach only considers the ratio of the laser power to the scan speed and does not capture the hatch spacing or layer thickness. Instead, DED machine parameters were simplified using a volumetric energy density which can be calculated according to Equation 3 [39]:

$$ED\left(\frac{J}{mm^3}\right) = \frac{L_P}{T_R H_S Z_S} \quad (3)$$

where ED is the energy density, L_P is the laser power, T_R is the traverse rate, H_S is the spacing of adjacent laser passes (xy-step size), and Z_S is the layer thickness (z-step size). Note that the powder feed rate (P_F), an important parameter in DED, is not accounted for in this ED calculation. Within the solid cube CCDs, the ED varied from 93 J/mm^3 to 1204 J/mm^3.

The effect of ED on specimen density is presented in Figure 5 where it is apparent that this trait improved with increasing EDs between 100-450 J/mm^3. Above 500 J/mm^3 there was minimal improvement in density and the data exhibited an asymptotic trend. Due to the formation of keyhole porosity, decreases in specimen density are commonly observed following a peak in density with ED [1]. This was not the case for Ti-55511 as high densities were achieved for specimens between 300-1200 J/mm^3.

 doi:10.20944/preprints202403.0498.v1

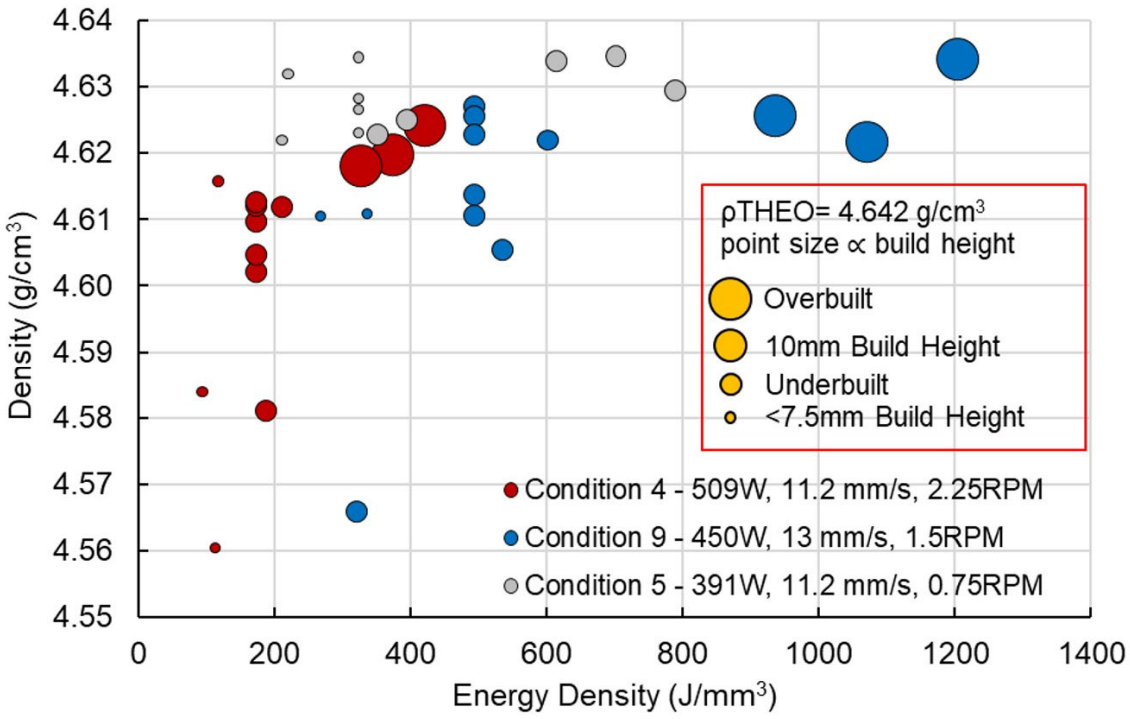

Figure 5. Density of DED Ti-55511 cube specimens versus energy density. The point sizes are proportional to the build height where smaller points represent under-building and larger points represent over-building relative to the programmed height.

The point sizes in Figure 5 are proportional to the build height of the cubes (i.e., small points represent under-building while large points represent over-building of the programmed height). The distribution of point sizes shows the general amount of underbuilding and overbuilding, with the majority of cube building successfully and only select samples failing to build at all (i.e., cube # 3 shown in Figure 4.).

Figure 5 also demonstrates that all cube specimens exhibited relative densities above 98% (4.55g/cm^3). Energy densities above 300J/mm^3 were required to achieve densities above 99.5% (4.62g/cm^3). A maximum density of 99.8% (4.633g/cm^3) was achieved in conditions 5 and 9 while condition 4 exhibited a maximum density of 99.6% (4.624g/cm^3). An energy density above 330J/mm^3 was required to avoid significant underbuilding, though some lower energy density specimens in condition 4 exhibited no underbuilding. Dense specimens (>99.5% density) with no underbuilding were deposited under each of the selected DED conditions implying that Ti55511 has a relatively wide DED processing window.

Although the specimen density appeared to trend with ED, variances in the density data were not entirely explained by the singular ED parameter. For example, cube 10 (ED = 321J/mm^3 and ϱ = 98.4%) and cube 33 (ED = 324J/mm^3 and ϱ = 99.8%) were deposited using similar ED, but employed unique L_P, P_F, and overlap parameters. Despite comparable ED, the lower laser power, powder feed rate and XY-overlap resulted in a higher density. This inferred that certain machine parameters, including P_F (which is not included in the ED model), may interact with one another, and influence Ti-55511 density.

The polished cross section of condition 5 (391 W, 11.2 mm/s, 0.75 RPM) printed with an X-Y overlap of 35% and Z-overlap of 10% (the CCD center point parameters) is shown in Figure 6. Few pores were visible in the cross section which supported the high measured density of 99.84% (4.634 g/cm^3).

 doi:10.20944/preprints202403.0498.v1

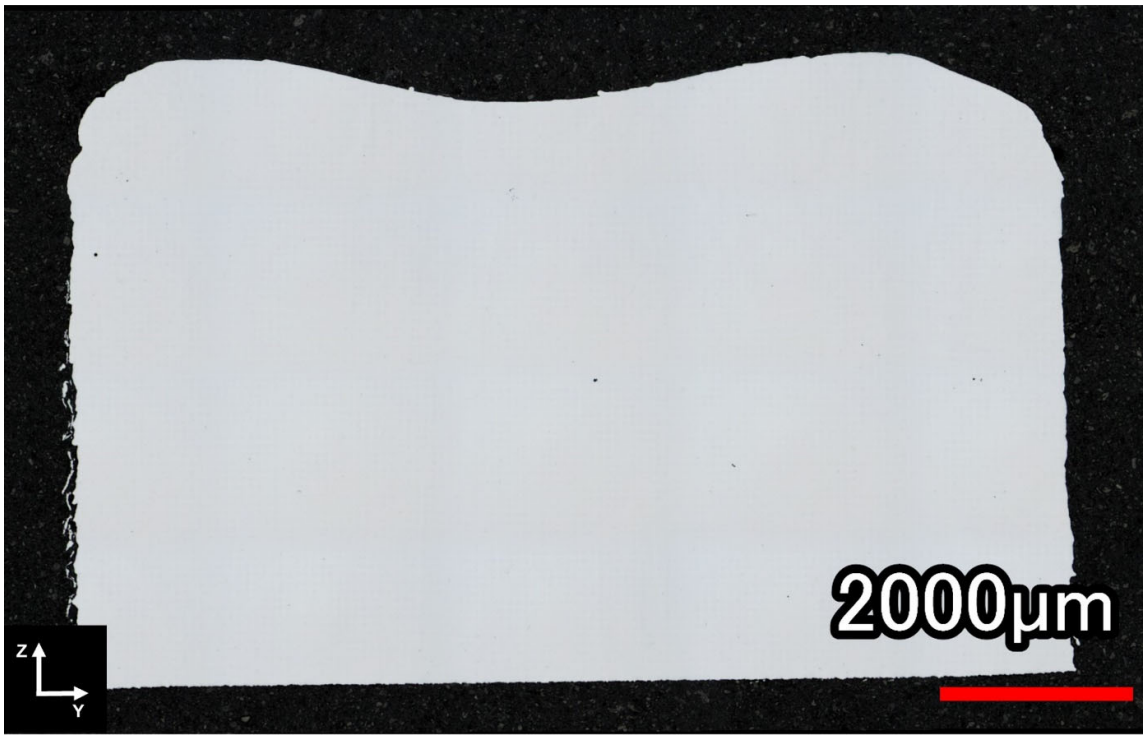

Figure 6. Polished cross section of condition 5 (391 W, 11.2 mm/s, 0.75 RPM) printed with an X-Y overlap of 35% and Z-overlap of 10%.

Each print condition was modeled individually to analyze the effects of the X-Y and Z-overlaps on the density of Ti-55511 deposits. An outlier printed with an X-Y overlap of 10% and Z-overlap of -20% was removed from condition 5 (391 W, 11.2 mm/s, 0.75 RPM) due to significant underbuilding and a 100% density measurement. A stepwise approach and a level of significance of 0.05 was used to test individual terms, their squares, and their interactions. Low p-values ($p < 0.001$) and insignificant lack-of-fit tests ($p > 0.05$) in conditions 4 and 9 suggested the models were statistically suitable to predict the density of cube deposits. The adjusted R-sq values were 93.0% and 64.0% for conditions 4 and 9, respectively. ANOVA for condition 5 returned high p-values, indicating that the variation in density was not attributable to the controlled parameters. This result makes sense because condition 5 had very little variation in density for different overlaps compared to the other two conditions (see Figure 5).

Statistical contour plots for the three build conditions with respect to the effective build rate are presented in Figure 7. The contour plots demonstrate that specimen density was proportional to the effective build rate across all three tested conditions. Specimen density increased with lower build rates while small X-Y overlaps, which have lower ED, resulted in lower densities. Specimen density was also more sensitive to the X-Y and Z overlap at the higher laser powers with condition 4 (509 W) exhibiting the largest range in densities (<4.57-4.63 g/cm^3). Larger X-Y overlaps have higher ED, increasing dilution and the ability to correct porosity in previously deposited layers. Condition 5 offered the lowest density variation over the range of effective build rates, inferring that lower powers can produce highly dense deposits with relatively low build times.

 doi:10.20944/preprints202403.0498.v1

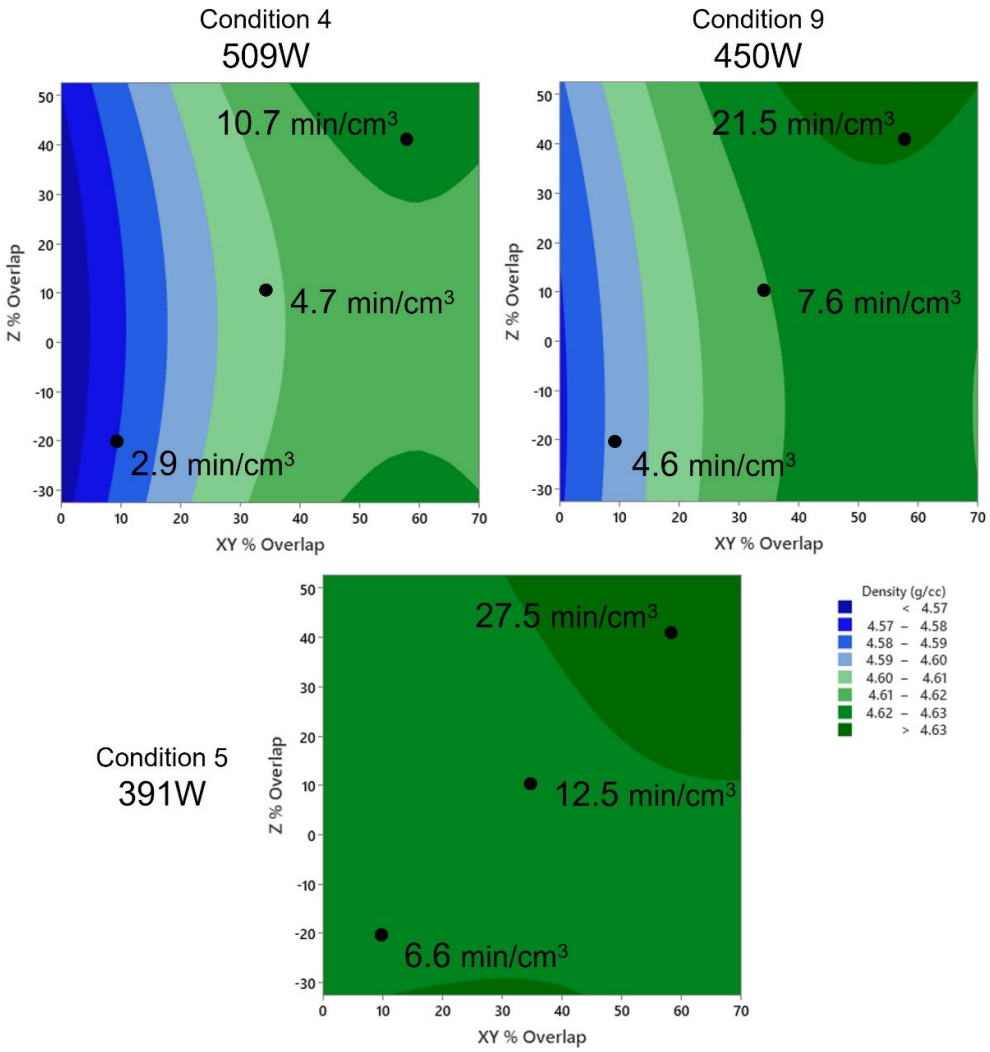

Figure 7. Density sensitivity with X-Y and Z-overlaps with respect to effective build rate using condition 4, 5, and 9.

All cube density data was combined, and a statistical model was fitted to evaluate the effect of all tested factors (laser power, traverse rate, powder feed rate, hatch spacing, and layer thickness). There were 13 individual data points for hatch spacing and layer thickness (including repeat center points) for each condition. In contrast, there were only 3 tested levels for the laser power, traverse rate, and powder feed rate, limiting the accuracy of their modeled effects due to the small sample size. Regardless, these parameters were included in the model as they could potentially provide useful information about the general behaviour of Ti-55511 deposition.

A backwards elimination stepwise approach was employed on all terms, their squares, and their interactions. The model had an adjusted R-sq value of 84%. Low p-values (<0.005) and insignificant lack-of-fit test (>0.05) showed that the model was statistically suitable. Hatch spacing and its square term were the only statistically significant terms in the resulting model (p-values of 0.002 and 0.000, respectively). Z_S was the next most significant term with a p-value = 0.013, followed by the interaction between H_S and Z_S. Parameters L_P and T_R as well as the interaction terms L_P*H_S, and H_S*Z_S, remained in the model but had p-values >0.005. The powder feed rate and remaining interactions either could not be estimated and were removed or were eliminated from the model having an alpha value >0.1. Given the limited test points for L_P, T_R, and P_F, it is not surprising that the most significant parameters in the model were those with the most data, H_S and Z_S. As expected, L_P, T_R, and P_F, and their interactions could not be attributed to variations in Ti-55511 density due to their limited sample size.

 doi:10.20944/preprints202403.0498.v1

The modeled effects of hatch spacing and layer thickness on Ti-55511 specimen density are presented in Figure 8. L_P, T_R, and Z_S had minimal effects on density (F-values of 1.23, 4.94, and 7.04, respectively) while the hatch spacing proved to have the largest effect (F-value=26.23).

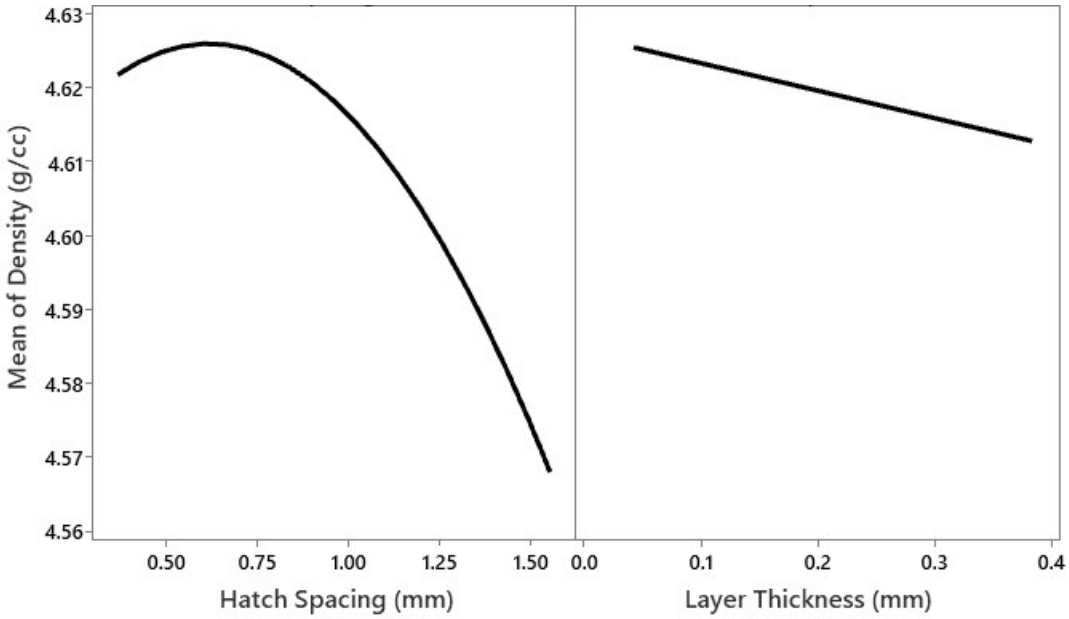

Figure 8. Effects of hatch spacing and layer thickness on Ti-55511 specimen density for conditions 4, 5, and 9.

The model suggested that the hatch spacing was attributable to variations in density. Hatch spacing had a parabolic relationship with density which exhibited a maximum between 0.5-0.75mm. Specimen density quickly deteriorated to a minimum of 4.560g/cm^3 (98.24%) as the hatch spacing was increased beyond 1mm. This result agrees with the measured density data where all densities above 4.633g/cm^3 (>99.80%) were achieved using low hatch spacings between 0.37mm and 0.80mm (corresponding to XY-overlaps of 35-70%). Similarly, all densities above 4.633g/cm^3 (>99.80%) were achieved with layer thicknesses below 0.2mm, which agrees with the predicted effect of layer thickness shown in Figure 8. The main effects of these parameters are aligned with the previously observed trends in the energy density data (see Figure 5). Small hatch spacings and layer thicknesses (high X-Y and Z-overlaps) increase energy density, which generally resulted in higher densities. In contrast, low laser powers decrease energy density, which resulted in lower densities except for the lowest power CCD (condition 5; 391W). Condition 5 had the highest densities, least variance, and was not explained by a statistical model. However, the model also suggested that the hatch spacing interacted with both laser power and layer thickness to influence specimen density. The interaction effects of hatch spacing with both layer thickness and hatch spacing are presented in Figure 9.

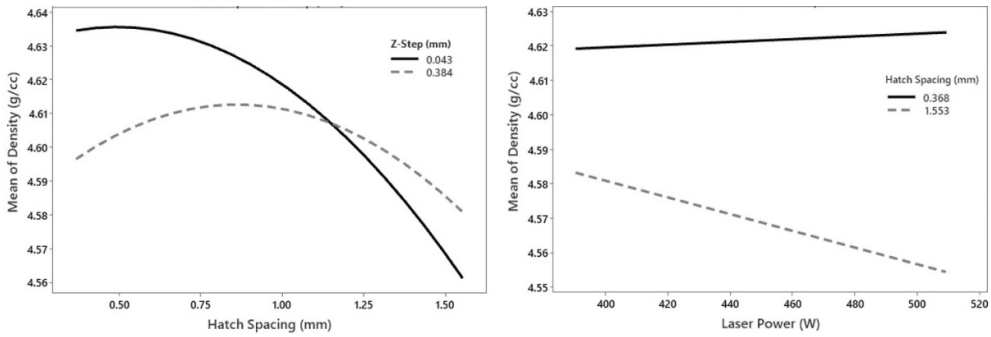

 doi:10.20944/preprints202403.0498.v1

Figure 9. Interaction effect between hatch spacing and layer thickness (left) as well as laser power and hatch spacing (right) on Ti-55511 specimen density for conditions 4, 5, and 9.

There was a clear interaction effect between the hatch spacing and layer thickness. Hatch spacing had a more dramatic effect on specimen density when a small layer thickness was employed, reaching high densities at low H_S values, and rapidly deteriorating as H_S was increased. In contrast, H_S had less influence on density at larger layer thicknesses. Laser power also interacted with hatch spacing, exhibiting more sensitivity to laser power at larger hatch spacings with high laser powers resulting in lower densities. At low hatch spacings (high XY-overlap), high densities could be achieved across the tested laser power range. The interaction between these parameters demonstrates that low H_S and Z_S can interact to achieve high densities while laser power is less critical at small H_S.

The powder feed rate is an important parameter not accounted for in the ED calculation (Equation 3). All specimens deposited when the powder feed rate was 0.75 RPM had > 99.5% density, suggesting that low powder feed rates generally help promote high densities in Ti-55511. Higher powder feed rates, which were employed at both higher laser power levels, were associated with lower densities. In a similar study on DED of dual phase steel, Sweet et al., also noted a decreased density with increased mass inputs (powder feed rates) [18]. This effect was attributed to an increase in the energy lost by the powder stream by either reflection, evaporation, or heating of unfused powder [18,40]. In DED, the presence of powder in the laser path can also intercept the energy input and shadow the substrate, contributing to the energy lost by the powder stream [40]. Similar to Sweet et al.'s work, the fraction of powder input to the system that absorbed energy but did not fuse to the substrate was increased at high powder feed rates, effectively reducing the energy input to the substrate and deposited powder. This theory is supported by the single track results shown in Table 3 where all powder feed rates ≤0.75 RPM exhibited >30% capture efficiency while higher powder feed rates generally exhibited <30% capture efficiency. This likely resulted in the reduced densities observed at both higher powder feed rate settings.

3.3. Microstructural Evaluation

Cube specimens printed under build conditions 4 and 5 were mounted and polished for metallurgical examination. Cross sections of as-built and stress relieved specimens printed under identical parameters are presented in Figure 10 for samples representing the center point of the CCDs (the condition to which the significance of changes was tested). The resulting as-built grain structures (Figure 10a,b) were quite different. Condition 4 (ED = 173 J/mm^3, 509 W, 11.2 mm/s, 2.25 RPM, H_S = 1.010 mm, Z_S = 0.261 mm) exhibited a nominally equiaxed grain structure while condition 5 (ED = 324 J/mm3, 391 W, 11.2 mm/s, 0.75 RPM, H_S = 0.796 mm, Z_S = 0.135 mm) manifested a highly columnar grain structure that extended through numerous build layers. Etching of the samples (Kroll's reagent) revealed the grain boundaries, alpha and beta phase contrast, and melt-track details. The bead size and layer thickness were notably larger in the higher power condition (509W, Condition 4), which is consistent with the single track bead height and width measurements. Samples stress relieved at 960°C for 1hr under high vacuum (Figure 10c,d) did not exhibit any obvious recrystallization or grain growth.

 doi:10.20944/preprints202403.0498.v1

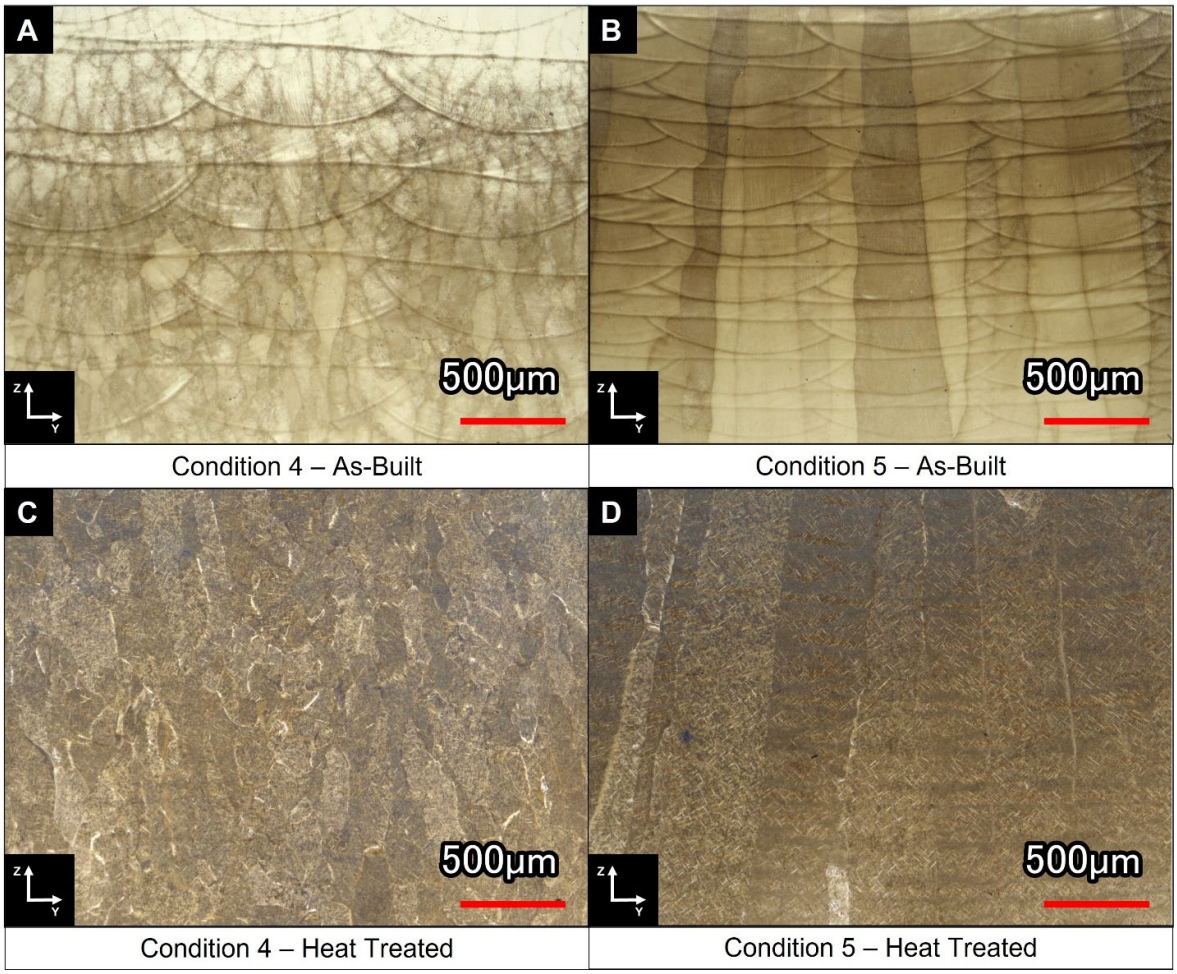

Figure 10. Microstructures of DED Ti-55511 cubes for print conditions 4 and 5 in the a), b) as-printed condition and c), d) heat treated condition (960°C for 1hr under high vacuum), respectively.

Higher magnification images of the as-built and stress relieved microstructures are presented in Figure 11. Areas of Widmanstatten and basket-weave type alpha phase are present under both conditions post-stress relieving, though condition 5 appeared to experience a higher degree of alpha phase coarsening and contained bands of basket-weave alpha. Grain boundary alpha was also observed in the stress relieved microstructures.

 doi:10.20944/preprints202403.0498.v1

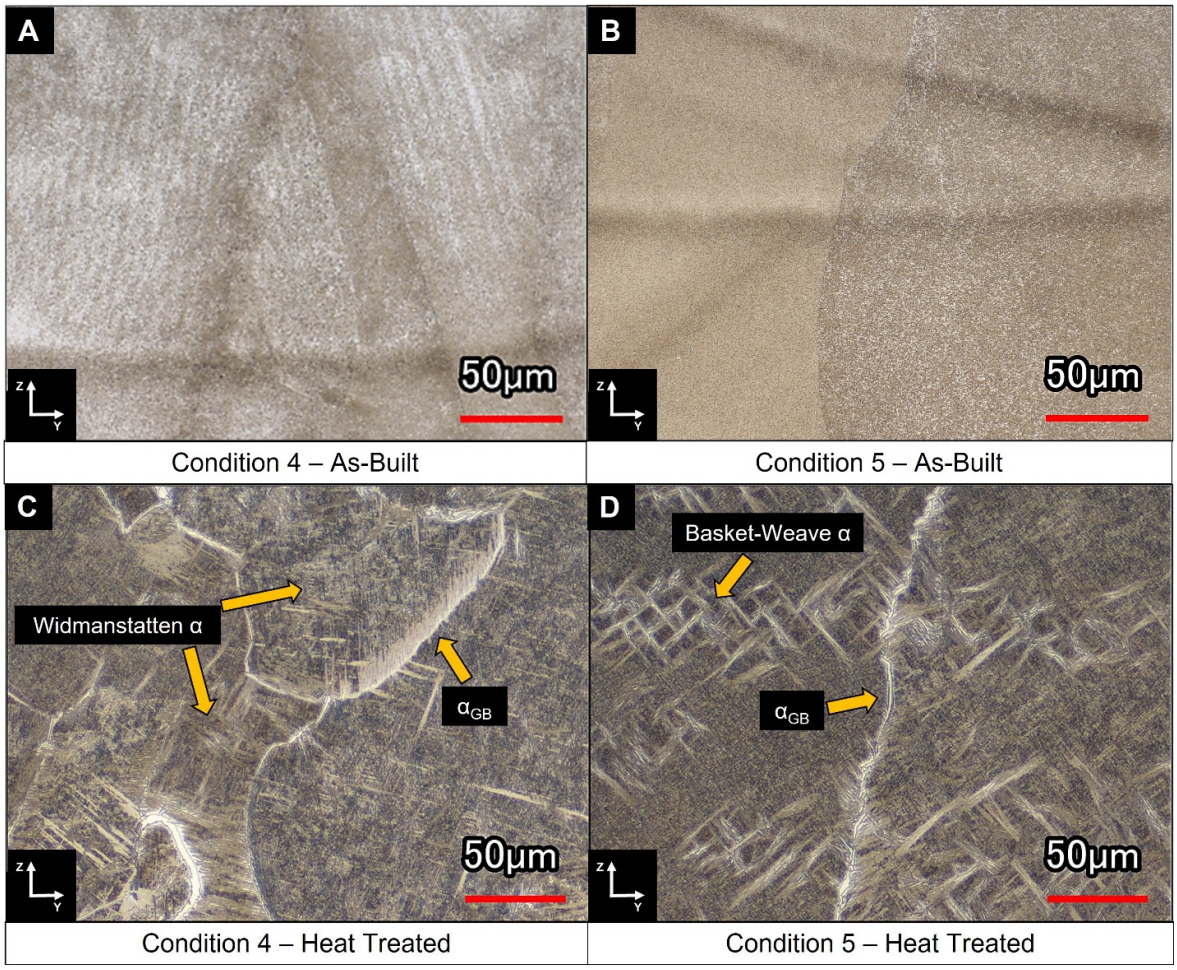

Figure 11. High magnification images of print conditions 4 and 5 in the a), b) as-printed and c), d) heat treated conditions, respectively.

A. Dass et al. described how DED process parameters influence the deposited microstructure [1]. Increases in T_R and P_F and decreases in L_P lead to lower thermal gradients, G (K/cm), between the melt pool and the solidified material. Lower thermal gradients give rise to higher solidification front velocities, R (cm/s), which result in higher degrees of nucleation and equiaxed microstructures [1]. The contrary promotes columnar growth due to less nucleation and a lower cooling rate while a mixed region exists between both regimes which contains a combination of equiaxed and columnar growth. The clear difference in grain structure between conditions 4 and 5 point to these deposition processes operating within two different grain structure regimes.

C. Liu et al. observed a mixed mode grain structure in laser melting deposition (LMD) processed Ti-55511 [6]. In their work, epitaxial growth occurred at the bottom of the melt pool due to heterogeneous nucleation promoted by the previously deposited layer. Equiaxed growth occurred at the top of the melt pool due to higher nucleation from the powder feed and the columnar to equiaxed transition (CET) caused by constitutional supercooling from solute segregation. As a result, each layer consisted of columnar grains at the bottom and equiaxed grains at the top in a bamboo-like morphology. Figure 10a,b exhibited entirely equiaxed and columnar structures, respectively. Although there was some localized evidence of epitaxial growth between successive layers in condition 4 (Figure 10a), the bulk of the deposited material had an equiaxed grain structure. Condition 5 (Figure 10b) was entirely columnar and showed no evidence of a CET.

Conditions 4 and 5 employed different L_P, P_F, H_S, and Z_S. Condition 4 used a high L_P and P_F which produced an equiaxed structure, suggesting that the high P_F promoted high nucleation and

 doi:10.20944/preprints202403.0498.v1

equiaxed growth despite a high laser energy input. Condition 4 also used relatively large H_S and Z_S (low X-Y and Z overlap), decreasing ED which manifested a lower thermal gradient and equiaxed structure. In contrast, condition 5 used a low L_P and P_F which produced a columnar structure, despite the use of a relatively low laser energy input. Condition 5 also employed a small H_S and Z_S (large X-Y and Z overlap), increasing ED which led to a higher thermal gradient and enhanced propensity for the observed columnar structure. Apparently, there is a change in the deposited structure over a small ED range (173-324 J/mm^3). This is consistent with the interaction effects of H_S and Z_S on the deposition process (see Figure 9) where small H_S and Z_S (higher ED) caused a different density response than large H_S and Z_S (lower ED). It is also important to highlight that the columnar structure was produced using a higher energy density (324 J/mm^3) than the equiaxed structure (173 J/mm^3).

In condition 4, the higher L_P was required to compensate for the additional powder mass flow and lower overlaps (higher H_S and Z_S). As a result, the overall ED is lower compared to condition 5, which used a lower laser power to account for a low powder mass flow and high heat accumulation in the deposited layer due to the higher overlaps. In either case, P_F evidently influences the deposited structure and, likely, specimen density in a similar manner as L_P.

Post-heat treatment microstructures of deposition conditions 4 and 5 are shown in Figure 12. Grain boundary alpha (α_{GB}) was present throughout both specimens and exhibited continuous and discontinuous features. Colonies of widmanstatten grain boundary alpha (α_{WGB}) were found throughout both deposition conditions. A basket weave microstructure of primary (α_P) and secondary (α_S) alpha was prominent within the beta grains. A thin precipitate free zone (PFZ) was also observed between the α_{GB}/α_{WGB} and the α_P/α_S regions.

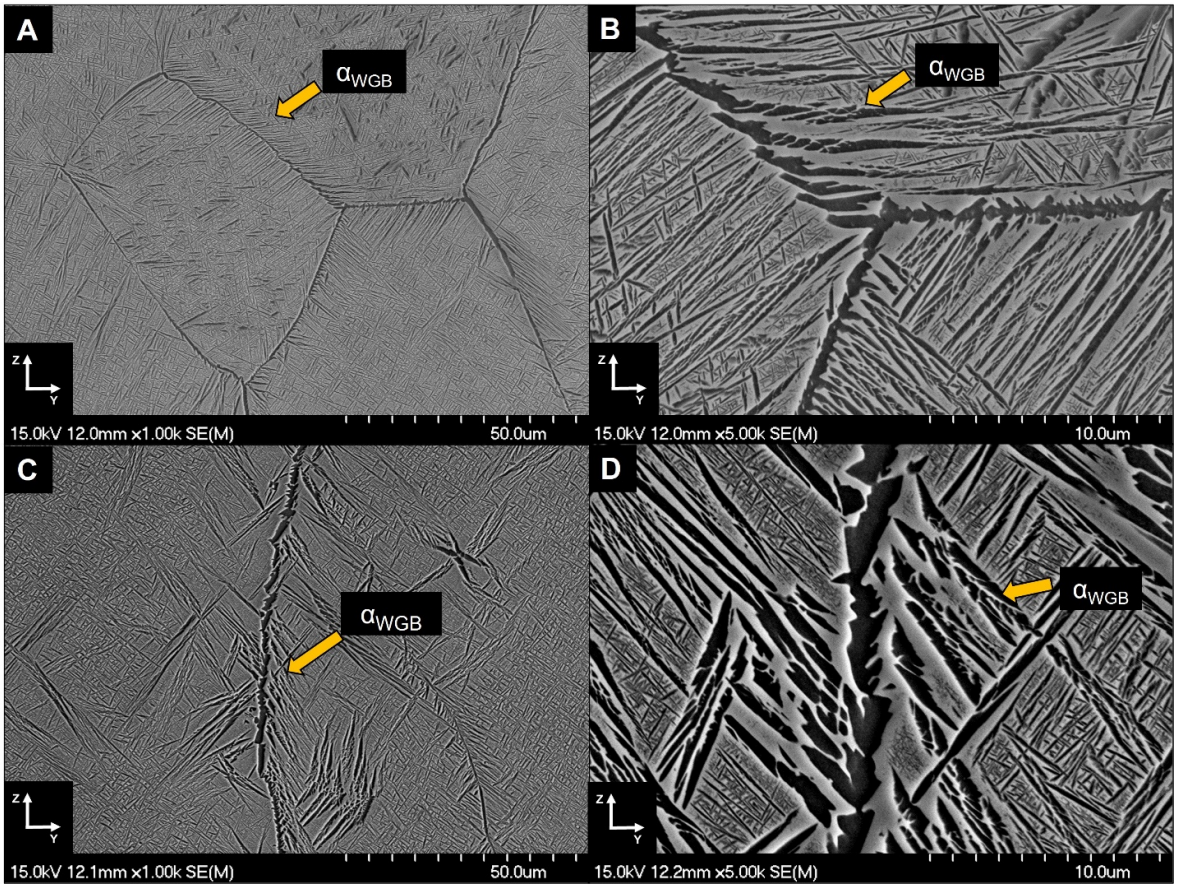

Figure 12. SEM micrographs of heat treated DED Ti-55511 cubes for print conditions 4 (a, b) and 5 (c, d).

The microstructures observed are consistent with the work of Liu et al., who studied the beta heat treatment of LMD Ti-55511 [5]. Their work demonstrated that as-printed Ti-55511 specimens

 doi:10.20944/preprints202403.0498.v1

contained linear grain boundary alpha (α_{LGB}) because of the complex thermal cycling during deposition. The presence of continuous films of α_{LGB} in as-printed Ti-55511 allowed intergranular crack propagation through the PFZs and resulted in low ductility (<5%). In contrast, the formation of herringbone and Widmanstatten alpha phase morphologies, α_{WGB}, which forms upon cooling from the β phase field, breaks up the PFZs and limits crack propagation, increasing the ductility. Therefore, a β heat treatment (above the β transus temperature, T_β = 880°C, for Ti-55511 [5]) is required to transform the retained α_{LGB} to α_{WGB} and improve the ductility of the material. The microstructures in Figure 12 were heat treated above the β transus (T_{HT} = 960°C) and exhibit the discontinuous grain boundary morphologies reported by Liu et al. which can lead to superior ductility.

3.4. Mechanical Properties

Tensile properties for specimens printed under conditions 4 and 5 are presented in Table 4. These two deposition conditions were selected for tensile testing due to their differing grain structures (see Figure 11). The presented data are an average of 2 or more individual tests and all specimens were tested in the stress-relieved condition (960°C for 1hr under high vacuum). Each deposition condition was printed utilizing both recycled argon (Recycled Ar) and a direct purge of argon (Direct Ar) to shield the melt pool. In the direct purge (Direct Ar) set-up, high purity Ar gas (99.999% Ar) was drawn directly from the compressed gas bank to supply the shield gas and powder feeder carrier gas. This approach ensures that high-purity Ar gas is being used to shield the melt pool during the printing process to minimize contamination. However, it is more economical to recycle the Ar shield gas using an argon recirculation system. By printing under both recycled Ar and direct Ar shield gas conditions, the impact of shield gas impurity content in the recycled Ar process could be assessed.

Specimens printed while continually recycling argon through the chamber, process shield gas, and powder feed exhibited acceptable ultimate tensile strength (UTS) and yield strength (YS) but poor ductility when compared with literature values [5,6]. The percent elongation for condition 4 was 2.7% while condition 5 had a higher ductility at 6.2%. The inferior ductility exhibited by condition 4 could be caused by a slightly lower density. Under the direct Ar condition, the specimens had lower UTS and YS, but were substantially more ductile and exceeded the elongation requirement in the literature [5,6]. The difference in elongation between the recycled Ar and direct Ar processing conditions is evident in the stress-strain curves presented in Figure 13. In general, specimen printed using recycled Ar had inferior ductility to those printed under direct purge conditions regardless of the print parameter set employed.

Table 4. Tensile properties for stress relieved specimens printed under conditions 4 (509W) and 5 (391W) using different shield gas sources.

Condition	Purge Gas Type	E (GPa)	Yield (MPa)	UTS (MPa)	EL (%)
4	Recycled Ar	92	1092	1167	2.7 ± 0.9
4	Direct Ar	88	960	1062	9.7 ± 1.8
5	Recycled Ar	84	1022	1138	6.2 ± 1.0
5	Direct Ar	86	952	1056	12.2 ± 0.0
[5,6]	N/A	-	≥1010	1080-1280	≥8

 doi:10.20944/preprints202403.0498.v1

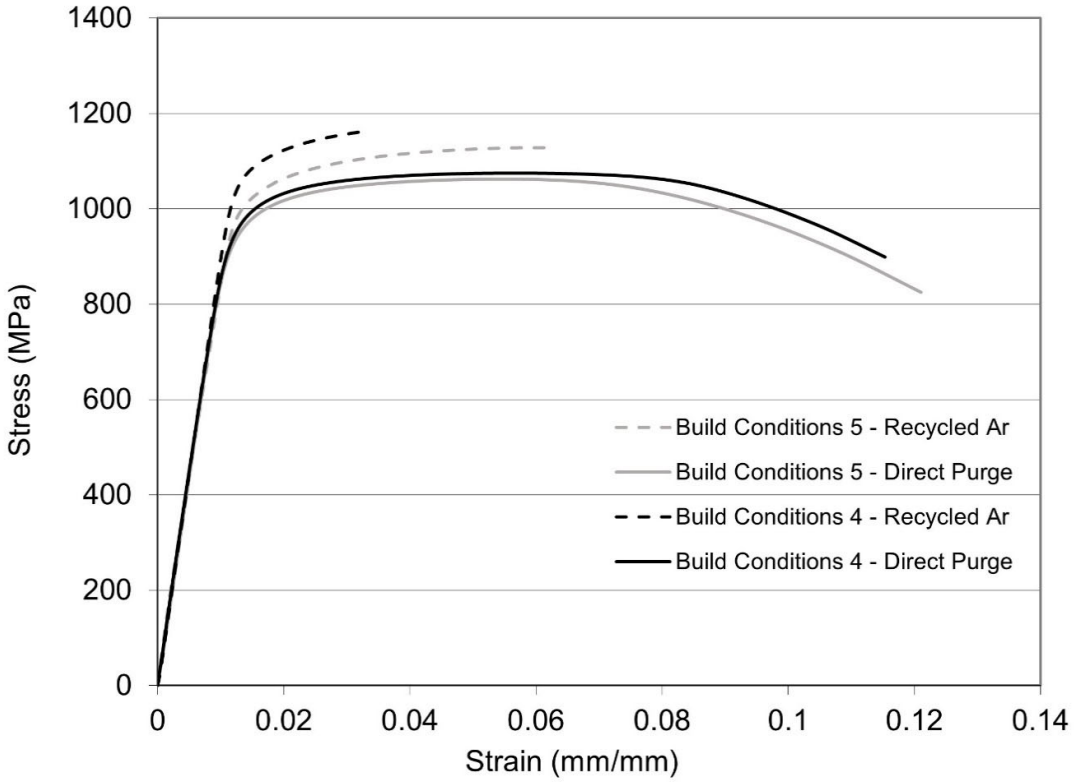

Figure 13. Stress-strain curves for the Ti-55511 tensile specimens fabricated using conditions 4 and 5 under both the recycled argon atmosphere and the direct purge atmosphere. All specimens were stress-relieved at 960°C for 1hr under high vacuum.

Titanium has a high affinity to oxygen, nitrogen, and carbon. These elements diffuse interstitially through the microstructure and can negatively impact the ductility [34,41]. Rousseau et al., highlighted that by increasing the oxygen content in Ti-6Al-4V up to a limit of 2000 ppm O_2, the tensile strength could be improved without negatively impacting the ductility [42]. However, controlling the impurity content during printing is critical because the interstitial content can cause embrittlement [43]. Generally, when high ductility and toughness are required, as is the case in most Ti-alloy aerospace applications, the interstitial content must be kept to acceptably low levels to prevent embrittlement [43].

The oxygen and nitrogen (ON) contents of the tensile specimens were measured to quantify and compare the impurity level imparted by the recycled and direct Ar process conditions. The results, presented in Figure 14, demonstrate that there was a significant amount of nitrogen pick-up during the deposition process when the argon purge gas was continually recycled. The Ti-55511 powder feedstock had 169 ppm N_2, but processing using the recycled Ar gas caused an increase to over 2500 ppm N_2. In contrast, the oxygen content was consistently 1100 ppm O_2 for the powder feedstock and all deposition conditions. The ductility achieved under the direct Ar purge condition is aligned with the results reported by Rousseau et al., where ductility could be maintained in Ti-6Al-4V with oxygen levels below 2000 ppm O_2 [42]. In the recycled Ar case, the accumulation of N_2 in the deposited Ti-55511 clearly caused embrittlement. Although this result may not be surprising, it highlights the importance of monitoring O and N impurity levels in the DED process environment for Ti alloys.

 doi:10.20944/preprints202403.0498.v1

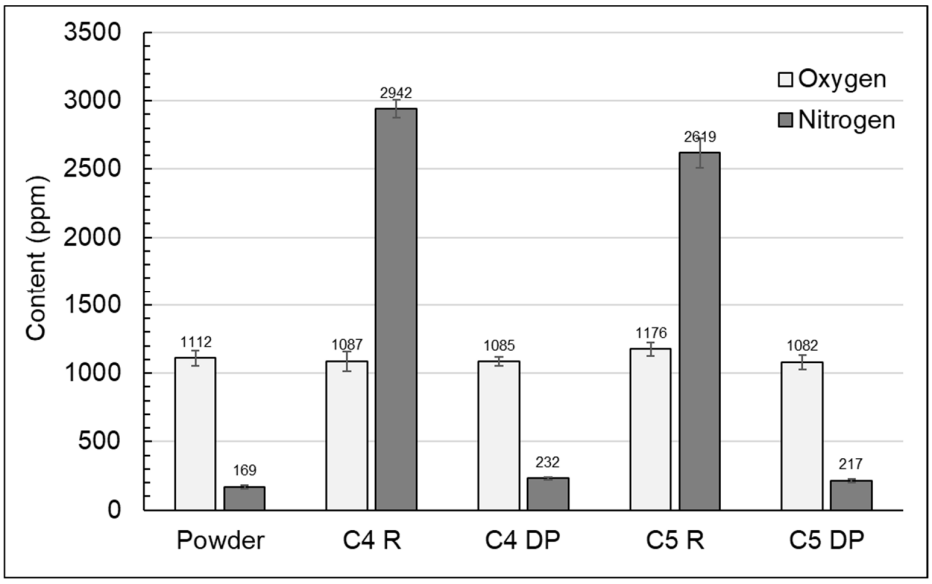

Figure 14. Oxygen and nitrogen contents of the as-received powder compared to tensile specimens printed under recycled argon (R) and direct purge argon (DP) for conditions 4 (C4) and 5 (C5).

The tensile specimen printed using recycled Ar exhibited elevated N_2 contents, but their O_2 contents were consistent with the level measured for the as-received Ti-55511 powder. Tensile specimen printed with the direct Ar showed no significant change in O or N content from the as-received powder. This result implies that the source of the N_2 contamination was in the Ar recirculation system. However, an air leak in the Ar recirculation system would have imparted both O_2 and N_2 to the material. Therefore, an alternate source of N_2 in the Ar recirculation system must have existed. To further investigate the source of the N_2 contamination, additional ON test pins were printed using deposition conditions 4 and 5 with both the recycled and direct purge Ar. Following these additional prints, the particulate filter in the Ar recirculation system was replaced and an additional set of ON test pins were printed using deposition conditions 4 and 5 with the recycled Ar. The ON results for these test pins are compared in Figure 15.

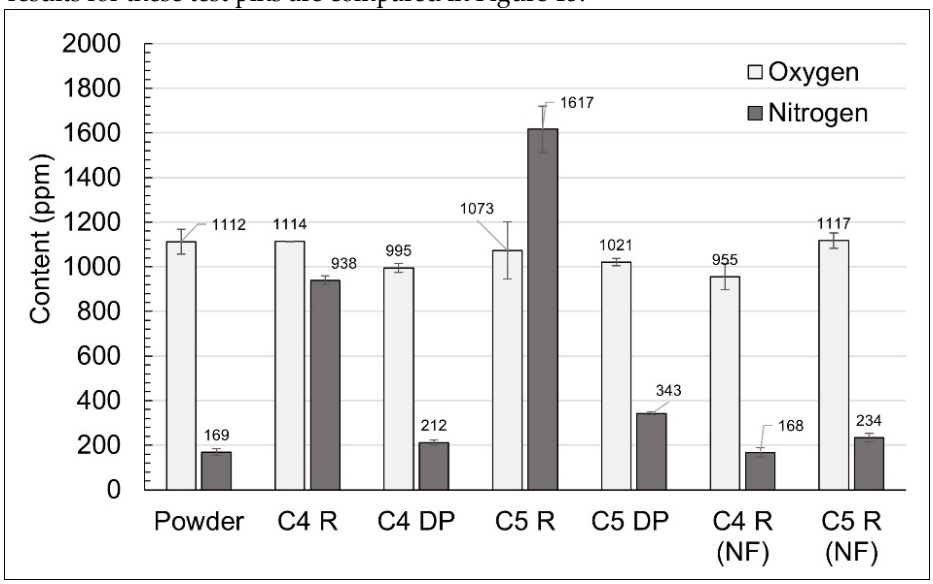

Figure 15. Oxygen and nitrogen contents of the as-received powder compared to Ti55511 pins printed under recycled argon (R) and direct purge argon (DP) for conditions 4 (C4) and 5 (C5). Specimen printed using a new argon recirculation system filter are denoted by "NF".

 doi:10.20944/preprints202403.0498.v1

The ON results from the Ti55511 test pins demonstrated that the N_2 pick-up observed in the tensile specimens (Figure 14) was repeatable and that the same trend was present in the ON test pins (Figure 15). Ti55511 pins printed using recycled Ar showed increased N_2 content while specimen printed with direct Ar showed no significant ON pick-up. When the particulate filter in the Ar recirculation system was replaced prior to printing, test pins printed with the recycled Ar no longer exhibited significant ON pick-up. Evidently, the observed N_2 pick-up was effectively mitigated by employing a new filter in the Ar recirculation system. The filter in the Ar recirculation system captures metal particulate formed during printing operations. It is postulated that accumulated metal particulate in the filter off-gassed N_2 into the recirculating Ar purge gas, causing the shield gas for the melt pool to contain elevated levels of N_2 which then contaminated the Ti55511 during printing.

The chemical composition of samples printed under DED conditions 4 and 5 are presented in Table 5. The compositions were nearly identical under both processing conditions and were within the acceptable compositional range. The composition of the printed material was also very similar to the as-received powder composition, exhibiting no major loss of alloying additions during the DED process or subsequent heat treatment.

Table 5. Composition of tensile specimens printed under DED conditions 4 and 5 compared to the wrought alloy composition from GOST 19807: 1991 [36].

	Composition (wt%)					
Material	Al	Cr	Fe	Mo	Ti	V
GOST 19807:1991	4.4-5.7	0.5-1.5	0.5-1.5	4.0-5.5	Bal.	4.0-5.5
Condition 4	5.11	1.06	1.11	4.55	83.36	4.82
Condition 5	5.15	1.06	1.12	4.57	83.28	4.81

Fracture surfaces of the four different tensile specimens are presented in Figure 16. The specimens printed using the recycled Ar process gas (Figure 16a,b) exhibited brittle, intergranular fractures while the direct Ar (Figure 16c,d) displayed a ductile, trans-granular fracture mode. The fracture surfaces for condition 4 and 5 were very similar under each processing gas set-up.

 doi:10.20944/preprints202403.0498.v1

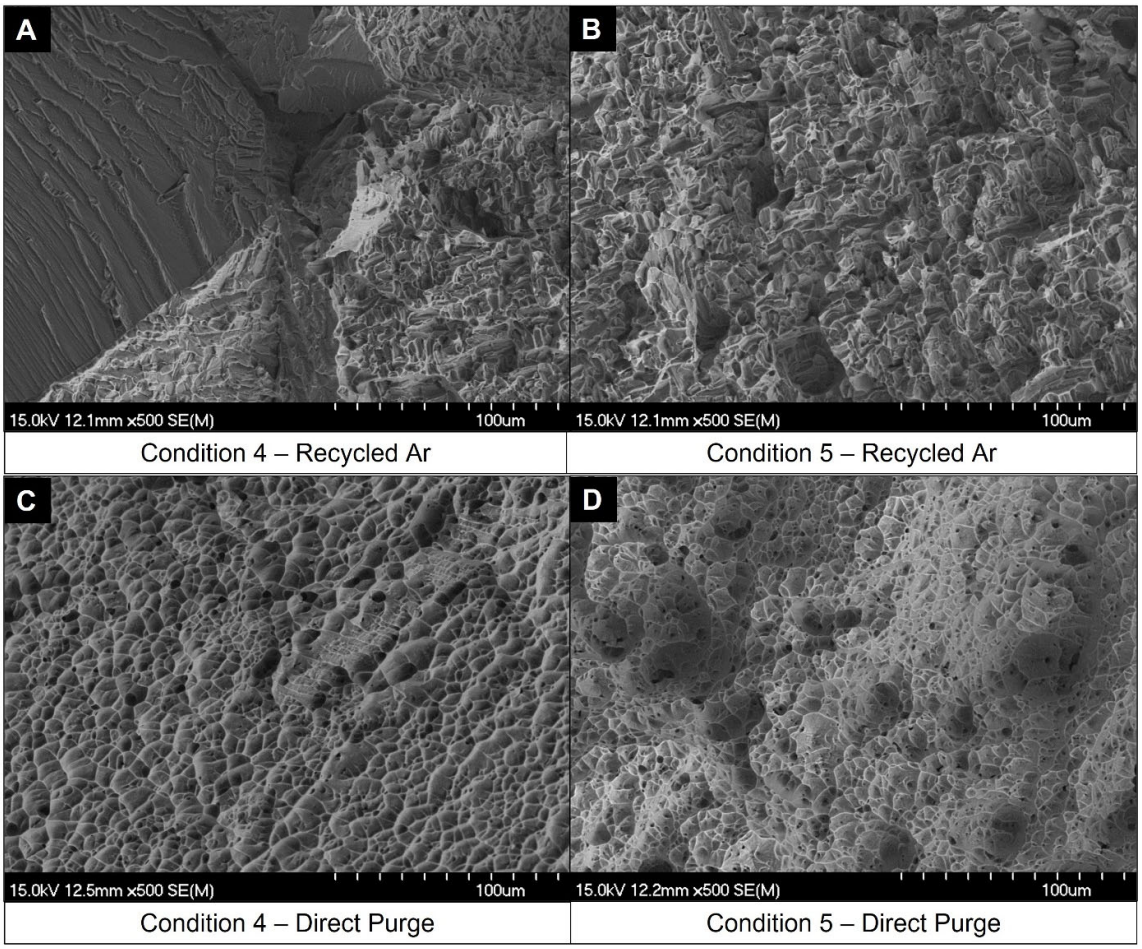

Figure 16. Fracture surfaces of DED Ti-55511 deposited under conditions 4 and 5 with recycled Ar (a,b) and direct Ar (c,d) process gasses, respectively.

The tensile specimens in this work were stress relieved above the beta transus temperature (β heat treatment). The specimens which were processed under the direct Ar process gas formed the beneficial α_{WGB} phase in the grain boundaries (see Figure 12) and displayed high ductility (See Table 4 and Figure 13). Liu et al. concluded that DED Ti-55511 required an intermediate heat treatment following the initial stress relieving/β heat treatment to coarsen the α_{WGB} phase and avoid an intergranular mode of fracture which would decrease the ductility [5]. By applying additional heat treatments, Liu et al. achieved 11% elongation in DED Ti-55511, which exceeds the requirements outlined in the literature [5]. In the present study, so long as the interstitial content was minimized, elongations between 10-12% were achieved after a single β heat treatment step above the β transus temperature. However, the UTS and YS were lower than those reported for DED Ti-55511 with additional heat treatment steps beyond the initial β heat treatment step. Additional aging steps at 750°C and 600°C promote the development of beneficially α_P and α_S, which increase strength by resisting dislocation motion and limiting crack propagation. Therefore, the development of α_P and α_S through subsequent aging treatments increases strength but is not detrimental to the ductility.

4. Conclusions

Multiple DED parameter sets were found to provide dense, defect free Ti-55511 deposits. The two-phase DOE approach was shown to be a valuable tool to rapidly infer build parameters for DED and the density/quality of the Ti-55511 builds were found to be proportional to the build rate. Two high density parameter sets were identified, one of which produced a columnar grain structure with

 doi:10.20944/preprints202403.0498.v1

the other producing an equiaxed grain structure. The tensile properties of DED Ti-55511 produced using the two optimal parameter sets agree with existing DED literature. Application of a single heat treatment (960°C for 1hr under high vacuum) above the beta transus temperature transformed retained linear grain boundary alpha phase, α_{LGB}, to a serrated Widmenstatten grain boundary morphology, α_{WGB}, improving the ductility of the material to acceptable elongations. Specimens processed using recycled argon gas had elevated nitrogen contents (> 2000 ppm), higher yield strength (1000-1100 MPa), but poor ductility (≤ 6%). Employing a new, clean gas filter in the argon recycling system effectively mitigated N_2 pick-up, maintaining N_2 levels comparable to the as-received Ti-55511 powder. Specimens processed using a direct argon gas purge exhibited little nitrogen pick-up, slightly lower yield strength (950-960 MPa), and acceptable ductility (≥ 8%). The interstitial impurity contents were found to be effectively alleviated with a direct purge of high purity Ar or by ensuring a new filter is employed if when using recycled Ar.

Author Contributions: Conceptualization, A.J. Rayner, G.A.W. Sweet, M. Habibnejad-Korayem, and D.P. Bishop; formal analysis, A.J. Rayner, G.A.W. Sweet, and O. Craig; investigation, A.J. Rayner, G.A.W. Sweet, and O. Craig; methodology, A.J. Rayner, G.A.W. Sweet, O. Craig, and D.P. Bishop; validation, A.J. Rayner, G.A.W. Sweet, and O. Craig; writing—original draft, A.J. Rayner; writing—review & editing, A.J. Rayner, O. Craig, M. Habibnejad-Korayem, and D.P. Bishop; resources, M. Habibnejad-Korayem and D.P. Bishop; supervision, M. Habibnejad-Korayem and D.P. Bishop; project administration, M. Habibnejad-Korayem and D.P. Bishop; funding acquisition, M. Habibnejad-Korayem and D.P. Bishop.

Funding: This research was funded by the Canadian Foundation for Innovation and Research Nova Scotia (grant #36245) as well as the Natural Sciences and Engineering Research Council of Canada via the Network for Holistic Innovation in Additive Manufacturing (grant # NETGP 494158-16).

Data Availability Statement: Data are available upon request from the corresponding authors.

Acknowledgments: The authors would like to graciously acknowledge the financial support provided by the Canadian Foundation for Innovation and Research Nova Scotia (grant #36245) as well as the Natural Sciences and Engineering Research Council of Canada via the Network for Holistic Innovation in Additive Manufacturing (grant # NETGP 494158-16) and GE for useful technical discussions.

Conflicts of Interest: The authors declare administrative support, equipment, drugs, or supplies, and writing assistance were provided by GE Additive. The authors declare financial support was provided by Natural Sciences and Engineering Research Council of Canada. The authors declare financial support was provided by Canadian Foundation for Innovation and Research Nova Scotia.

References

1. A. Dass, A. Moridi, State of the art in directed energy deposition: from additive manufacturing to materials design, Coatings. 9 (2019) 418. https://doi.org/10.3390/coatings9070418.
2. I. Gibson, D. Rosen, B. Stucker, Additive Manufacturing Technologies, second ed., Springer, NY, 2015. https://doi.org/10.1007/978-1-4939-2113-3.
3. E. Toyserkani, D. Sarker, O. Obehi Ibhadode, F. Liravi, P. Russo, K. Taherkhani, Metal Additive Manufacturing, John Wiley and Sons, 2022.
4. M. J. Kim, C. Saldana, Thin wall deposition of IN625 using directed energy deposition, J. Manuf. Process. 56 (2020) 1366-1373. https://doi.org/10.1016/j.jmapro.2020.04.032.
5. C. Liu, L. Yu, A. Zhang, X. Tian, D. Liu, S. Ma, Beta heat treatment of laser melting deposited high strength near β titanium alloy, Mater. Sci. Eng. A. 673 (2016) 185–192. https://doi.org/10.1016/j.msea.2016.07.027.
6. C. M. Liu, H. M. Wang, X. J. Tian, H. B. Tang, D. Liu, Microstructure and tensile properties of laser melting deposited Ti-5Al-5Mo-5V-1Cr-1Fe near β titanium alloy, Mater. Sci. Eng. A. 586 (2013) 323–329. https://doi.org/10.1016/j.msea.2013.08.032.
7. M. N. Ahsan, A. J. Pinkerton, R. J. Moat, J. Shackleton, A comparative study of laser direct metal deposition characteristics using gas and plasma-atomized Ti-6Al-4V powders, Mater. Sci. Eng. A. 528 (2011) 7648–7657. https://doi.org/10.1016/j.msea.2011.06.074.
8. C. Qiu, G. A. Ravi, C. Dance, A. Ranson, S. Dilworth, M. M. Attallah, Fabrication of large Ti-6Al-4V structures by direct laser deposition, J. Alloys Compd. 629 (2015) 351–361. https://doi.org/10.1016/j.jallcom.2014.12.234.
9. J. Yu, M. Rombouts, G. Maes, F. Motmans, Material properties of Ti6Al4V parts produced by laser metal deposition, Phys. Procedia. 39 (2012) 416–424. https://doi.org/10.1016/j.phpro.2012.10.056.

10. Y. Zhai, D. A. Lados, E. J. Brown, G. N. Vigilante, Fatigue crack growth behavior and microstructural mechanisms in Ti-6Al-4V manufactured by laser engineered net shaping, Int. J. Fatigue. 93 (2016) 51–63. https://doi.org/10.1016/j.ijfatigue.2016.08.009.
11. B. E. Carroll, T. A. Palmer, A. M. Beese, Anisotropic tensile behavior of Ti-6Al-4V components fabricated with directed energy deposition additive manufacturing, Acta Mater. 87 (2015) 309–320. https://doi.org/10.1016/j.actamat.2014.12.054.
12. J. S. Keist, T. A. Palmer, Role of geometry on properties of additively manufactured Ti-6Al-4V structures fabricated using laser based directed energy deposition, Mater. Des. 106 (2016) 482–494. https://doi.org/10.1016/j.matdes.2016.05.045.
13. ASM Metals Handbook Volume 2: Properties and Selection: Nonferrous Alloys and Special-Purpose Materials, second ed. ASM International, OH, 1990.
14. P. J. Bania, Beta titanium alloys and their role in the titanium industry, JOM. 46 (1994) 16–19. https://doi.org/10.1007/BF03220742.
15. T. Maimaitiyili, K. Mosur, T. Kurzynowski, N. Casati, H. Van Swygenhoven, Phase studies of additively manufactured near beta titanium alloy-Ti55511, Materials. 13 (2020) 1723. https://doi.org/10.3390/ma13071723.
16. T. Kurzynowski, M. Madeja, R. Dziedzic, K. Kobiela, The effect of EBM process parameters on porosity and microstructure of Ti-5Al-5Mo-5V-1Cr-1Fe alloy, Scanning. 2019 (2019). https://doi.org/10.1155/2019/2903920.
17. D. Li et al., Additive manufacturing of high strength near β titanium alloy Ti-55511 by engineering nanoscale secondary α laths via in-situ heat treatment, Mater. Sci. Eng. A. 814 (2021) 141245. https://doi.org/10.1016/j.msea.2021.141245.
18. G. A. W. Sweet, I. W. Donaldson, C. T. Schade, M. Y. Amegadzie, D. P. Bishop, Laser free-form fabrication of dual phase DP600 steel using water atomized feedstock powder, Addit. Manuf. 47 (2021) 102357. https://doi.org/10.1016/j.addma.2021.102357.
19. D. C. Montgomery, Design and Analysis of Experiments, eighth ed., John Wiley & Sons, 2013.
20. G. Wang et al., Process optimization and mechanical properties of oxide dispersion strengthened nickel-based superalloy by selective laser melting, Materials and Design 188 (2020) 108418.
21. M. Vilanova, R. Escribano-Garcia, T. Guraya, M. San Sebastian, Optimizing Laser Powder Bed Fusion Parameters for IN-738LC by Response Surface Method, Materials 13 (2020) 4879. https://doi.org/10.3390/ma13214879.
22. G. A. W. Sweet, I. W. Donaldson, C. T. Schade, D. P. Bishop, Laser-Based Directed Energy Deposition (L-DED) Processing of Water Atomized 42CrMo4 Powder, Laser in Manufacturing and Materials Processing 10 (2023) 32-63. https://doi.org/10.1007/s40516-022-00196-0.
23. Cao X, Wanjara P, Gholipour J, Wang Y (2019) Laser-Additive Repair of Cast Ni–Al–Bronze Components. In: TMS 2019 148th Annual Meeting & Exhibition Supplemental Proceedings. The Minerals, Metals & Materials Series. Springer, Cham. https://doi.org/10.1007/978-3-030-05861-6_19
24. A. Pfaff, M. Jacklein, M. Schlager, W. Harwick, K. Hoschke, F. Balle, An Empirical Approach for the Development of Process Parameters for Laser Powder Bed Fusion, Materials 13 (2020) 5400. https://doi.org/10.3390/ma13235400.
25. B. Fotovvati, M. Balasubramanian, E. Asadi, Modeling and Optimization Approaches of Laser-Based Powder-Bed Fusion Process for Ti-6Al-4V Alloy, Coatings 10 (2020) 1104. https://doi.org/10.3390/coatings10111104.
26. N. Gosse, Directed Energy Deposition Processing of Alpha-Beta, Near-Alpha, and Beta Titanium Alloys, Dalhousie University, Halifax, 2022.
27. W. D. Callister Jr., D. G. Rethwisch, Materials Science and Engineering—An Introduction, tenth ed., John Wiley and Sons, NJ, 2018.
28. S. Wolff, T. Lee, E. Faierson, K. Ehmann, J. Cao, Anisotropic properties of directed energy deposition (DED)-processed Ti–6Al–4V, J. Manuf. Process. 24 (2016) 397–405. https://doi.org/10.1016/j.jmapro.2016.06.020.
29. Q. Zhang, J. Chen, H. Tan, X. Lin, W Huang, Microstructure evolution and mechanical properties of laser additive manufactured Ti–5Al–2Sn–2Zr–4Mo–4Cr alloy, Trans. Nonferrous Met. Soc. China. 26, (2016) 2058–2066. https://doi.org/10.1016/S1003-6326(16)64300-5.
30. Y. Zhu, X. Tian, J. Li, H. Wang, The anisotropy of laser melting deposition additive manufacturing Ti-6.5Al-3.5Mo-1.5Zr-0.3Si titanium alloy, Mater. Des. 67 (2015) 538–542. https://doi.org/10.1016/j.matdes.2014.11.001.
31. X. Zhou et al., Mechanical properties, corrosion behavior and cytotoxicity of Ti-6Al-4V alloy fabricated by laser metal deposition, Mater. Charact. 179 (2021) 111302. https://doi.org/10.1016/j.matchar.2021.111302.
32. Q. Zhang, J. Chen, Z. Zhao, H. Tan, X. Lin, W. Huang, Microstructure and anisotropic tensile behavior of laser additive manufactured TC21 titanium alloy, Mater. Sci. Eng. A. 673 (2016) 204–212. https://doi.org/10.1016/j.msea.2016.07.040.

 doi:10.20944/preprints202403.0498.v1

33. J. D. Cotton et al., State of the art in beta titanium alloys for airframe applications, JOM. 67 (2015) 1281–1303. https://doi.org/10.1007/s11837-015-1442-4.
34. Gerd Lütjering, J. C. Williams, Titanium, second ed., Springer Berlin, Heidelberg, 2007. https://doi.org/10.1007/978-3-540-73036-1.
35. H. Deng et al., Microstructure and mechanical properties of as-deposited and heat treated Ti–5Al–5Mo–5V–3Cr–1Zr (Ti-55531) alloy fabricated by laser melting deposition, J. Alloys Compd. 810 (2019) 151792. https://doi.org/10.1016/j.jallcom.2019.151792.
36. GOST, Wrought Titanium and Titanium Alloys. Grades, 19807 (1991).
37. MPIF, Method for determination of density of compacted or sintered powder metallurgy (PM) products MPIF Standard 42, MPIF, 2008.
38. MPIF, Method for determination of tensile properties of powder metallurgy (PM) materials, MPIF Standard 10, MPIF, 2016.
39. D. Gu, Y. Shen, Effects of processing parameters on consolidation and microstructure of W–Cu components by DMLS, J. Alloys Compd. (2009) 107–115. https://doi.org/https://doi.org/10.1016/j.jallcom.2008.05.065.
40. F. Lia, J. Park, J. Tressler, R. Martukanitz, Partitioning of laser energy during directed energy deposition, Addit. Manuf. 18 (2017) 31-39. http://dx.doi.org/10.1016/j.addma.2017.08.012.
41. H. R. Ogden, R. I. Jaffee, The effects of carbon, oxygen and nitrogen on the mechanical properties of titanium and titanium alloys, Battelle Memorial Inst. Titanium Metallurgical Lab, United States, 1955. https://doi.org/10.2172/4370612.
42. J. Nicolas Rousseau, A. Bois-brochu, C. Blais, Effect of oxygen content in new and reused powder on microstructural and mechanical properties of Ti6Al4V parts produced by directed energy deposition, Addit. Manuf. 23 (2018) 197–205. https://doi.org/10.1016/j.addma.2018.08.011.
43. ASM Metals Handbook Volume 2: Properties and selection: nonferrous alloys and special-purpose materials, second ed., ASM International, OH, 1990, pp. 1790-1791.